

A Nonhydrostatic and Mass Conserving Ground-to-Thermosphere Dynamical Core based on Specific Internal Energy

James F. Kelly^{a,*}, Felipe A. V. de Bragança Alves^{b,**}, John T. Emmert^a, Stephen D. Eckermann^a, Francis X. Giraldo^b, P. Alex Reinecke^c

^a*Space Science Division, U.S. Naval Research Laboratory, Washington, DC, U.S.*

^b*Department of Applied Mathematics, Naval Postgraduate School, Monterey, CA, U.S.*

^c*Marine Meteorology Division, U.S. Naval Research Laboratory, Monterey, CA, U.S.*

Abstract

This paper presents the development of a deep-atmosphere, nonhydrostatic dynamical core (DyCore) targeted towards ground-thermosphere atmospheric prediction. This DyCore is based on a novel formulation of the specific internal energy equation (SIEE), which, unlike standard potential temperature formulations, is valid for variable composition atmospheres. Two versions of a SIEE are derived from basic principles. The first version, which uses a product-rule (PR) continuity equation, contains an additional compressible term and does not conserve mass. The second version, which does not use the product-rule (No-PR) in the continuity equation, contains two compressible terms and conserves mass to machine precision regardless of time truncation error. The pressure gradient and gravitational forces in the momentum balance equation are formulated in a manner appropriate for HA applications and the spectral element method (SEM) is used with Implicit-Explicit (IMEX) and Horizontally Explicit Vertically Implicit (HEVI) time-integration. These new equation sets were implemented in two U. S. Navy atmospheric models: the Nonhydrostatic Unified Model of the Atmosphere (NUMA) and the Navy Environmental Prediction sysTem Using a Nonhydrostatic Core (NEPTUNE). Numerical results using a nonhydrostatic and hydrostatic baroclinic instability, a balanced zonal flow, and HA mountain wave experiments are shown. These results are compared to existing deep-atmosphere dynamical cores, indicating that the proposed discretized IEE equation sets are viable next-generation ground-to-thermosphere DyCores.

Keywords: compressible Euler equations, specific internal energy, variable composition, numerical weather prediction, space weather, spectral element method, time-integration, mass conservation

Distribution Statement A: Approved for public release; distribution is unlimited

*Corresponding author

**Now at Instituto de Matemática e Estatística, Universidade de São Paulo, Brazil

Email addresses: james.kelly@nrl.navy.mil (James F. Kelly), favbalves@gmail.com (Felipe A. V. de Bragança Alves), fxgirald@nps.edu (Francis X. Giraldo)

1. Introduction

The thermosphere, extending from approximately 100 km to 600 km, is a hot, rarefied layer of the atmosphere which contains a charged layer known as the ionosphere. The thermosphere is driven from above by solar activity and from below by waves emanating from the lower atmosphere as well as by the ionosphere. In order to understand this complex interplay between the thermosphere, the ionosphere, and the lower atmosphere, the U. S. Navy recently built a coupled thermosphere-ionospheric prediction system (SEPHIR). During this project, we developed a whole atmosphere model [3] by extending the the Navy Environmental Prediction sysTEM Utilizing a Nonhydrostatic CorE (NEPTUNE) [39, 59] into the upper thermosphere. Much of the initial research was conducted in the Nonhydrostatic Unified Model of the Atmosphere (NUMA) [18], which shares many of the same numerical methods as NEPTUNE and serves as a prototype for the NEPTUNE model. NUMA is a research-oriented CFD code based on element-based Galerkin (EBG) methods [27, 37].

A fundamental problem in building a whole atmosphere model is the choice of equation set. Many NWP models utilize a (virtual) potential temperature equation, which is appropriate for a well-mixed atmosphere with uniform composition. Since potential temperature satisfies a transport equation, this choice is relatively simple and inexpensive from a computational point of view; however, the atmosphere above the homopause (~ 100 km), is not well-mixed and hence is comprised of variable composition, so potential temperature cannot be used without significant modifications [31, 10]. An alternative approach is specific enthalpy [4], which is used in the Whole Atmosphere Model (WAM). Yet another approach is specific total energy, which is valid for both variable composition and moist atmospheres [47].

Several nonhydrostatic high-altitude (HA) atmosphere models are now available. The global ionosphere thermosphere model (GITM) [40] solves the deep-atmosphere, nonhydrostatic Navier-Stokes equations using explicit time-integration for multiple species using a lower boundary near 100 km. GITM has since been adapted for the Martian atmosphere (M-GITM) [6] and the Jovian atmosphere (J-GITM) [7]. Efforts to adapt global numerical weather prediction (NWP) models for high altitude applications, such as space weather, have been underway for several years [26]. Initial efforts to extend the UK Met Office’s nonhydrostatic ENDGame [58] to a lid height of 500 km are summarized in [21]. Nonhydrostatic models support vertically propagating acoustic and gravity waves that grow exponentially with respect to height; these waves must be controlled numerically to keep the model stable with lid heights in the thermosphere. These issues are explored both analytically and numerically using both a 1D and 3D version of ENDGame’s dynamical core in Griffin’s Ph.D. thesis[20]. The ICOSahedral Non-hydrostatic (ICON) model from the German Weather Service (DWD) is extended to a model lid of 150 km lid in [5]. The atmospheric component of the NCAR Model for Prediction Across Scales (MPAS-A) has also been extended into the upper atmosphere. The deep-atmosphere aspect of this development is documented in [44], while HA applications, including diurnal heating and mountain wave tests, are discussed in [31] and [29].

Mass conservation is perhaps the most important invariant for the lower and middle

atmosphere. As discussed in [49], mass conservation is a key ingredient to ensure accurate forecasts, such as correctly diagnosing surface pressure. Although a small amount of mass in the upper atmosphere may escape/re-enter if a given molecule has sufficient velocity to escape the gravitational attraction of the earth, the mass loss in the lower and middle atmosphere is essentially zero. A gradual, secular loss of mass may distort the resolved dynamics over long term integrations. In addition, accurate surface pressure prediction depends on a proper mass budget [49]. Finally, mass conservation is a prerequisite for conserving other invariants, such as momentum and total energy. Hence, mass conservation in a DyCore is highly desirable as reflected by next-generation NWP [36] and HA [44] Dycores.

This paper documents the development of a new nonhydrostatic dynamical core (DyCore), based on a new formulation of the specific internal energy equation (SIEE) and the spectral element method (SEM), appropriate for both low-altitude and high-altitude (HA) atmospheric prediction. We chose SIEE since a) it naturally accounts for both moisture in the lower atmosphere and variable composition in the upper atmosphere, and 2) the resulting SIEE is similar to the θ equation, thereby requiring only minimal changes to the DyCore. The HA DyCore should resolve both low-altitude, tropospheric dynamics and high-altitude, thermospheric dynamics. In particular, we require our model to model deep-atmosphere, nonhydrostatic dynamics in the whole atmosphere, handle variable-composition in the HA regime, and conserve mass if a rigid boundary condition (BC) is enforced on both the lower and upper boundaries.

In Section 2, two versions of an SIEE are derived from the first law of thermodynamics and the continuity equation. The pressure gradient and gravitational forces are formulated in a manner appropriate for HA applications where density becomes highly rarefied. In Section 3, the SEM on a hexahedral mesh is briefly described, along with the metric terms and time-integrators used in two U. S. Navy atmospheric models: NUMA and NEPTUNE. Section 4 shows numerical results from this prototype DyCore using NUMA, including mass-conservation results, while HA numerical results using the NEPTUNE DyCore are shown in Section 5. Energy conservation is discussed in Section 6, while conclusions are presented in 7.

2. Specific Internal Energy Equation (SIEE)

2.1. Motivation

The proposed high-altitude dynamical core (DyCore) should have the following features: 1) deep-atmosphere dynamics, 2) nonhydrostatic, 3) variable gravitational acceleration, and 4) variable composition. The first three requirements are relatively straightforward to satisfy. Unlike the traditional shallow-atmosphere approximation, deep-atmosphere equations sets do not assume that the radial distance from a given grid-point to the center of the earth is constant. In addition, no approximations in either the spherical metric terms or Coriolis force are assumed. Modern nonhydrostatic dynamical cores do not assume hydrostatic balance in the vertical, yielding a prognostic equation for vertical velocity. Nonhydrostatic effects in the upper atmosphere, caused by intense heating [9], are physically important. Finally, the

acceleration of gravity varies by about twenty percent between the ground and the exobase (~ 500 km).

Both NUMA [18] and NEPTUNE [39] are based on the nonhydrostatic compressible Euler equations formulated in Cartesian coordinates. Hence, they are both deep-atmosphere and nonhydrostatic by construction. As shown in Section 2.3, adding variable gravity is relatively straightforward. Adapting NUMA and NEPTUNE to a variable composition atmosphere is more challenging, however. Due to the absence of turbulent mixing above 100 km, the mass-weighted specific gas constant R and specific heats c_v and c_p may vary with position and time. As a result, the standard potential temperature equation used in NWP is not valid. There are several approaches for accounting for variable composition, including adding a prognostic equation for the Poisson ratio $\kappa = R/c_p$ [31], specific enthalpy [4], total internal energy [50], the recently proposed hybrid virtual potential temperature (HPVT) equation [10], or using a specific internal energy equation (SIEE). We chose the SIEE approach in this paper for the relative simplicity, the minimal changes required in an existing θ -based Dycore, and efficiency concerns.

In addition, molecular viscosity and thermal conductivity play a major role in upper atmosphere dynamics. In the present study, we focus on the inviscid part of dynamics, and plan on discussing an implicit viscosity scheme in future work. We also neglect the presence of moisture in the troposphere.

2.2. Derivation

In this subsection, we derive two prognostic equations for specific internal energy from first principles. The resulting SIEEs are valid for variable composition atmospheres and hence appropriate for HA numerical models. The specific internal energy is defined as $e_i = c_v T$, where $c_v = \sum_i q_i (c_v)_i$ is the mass-weighted specific heat at constant volume, where q_i is the mass ratio of constituent species i and $(c_v)_i$ is the corresponding specific heat at constant volume for this species. The mass-weighted specific heat may vary with respect to both position and time in the upper atmosphere due to variation in composition. As part of the derivation, we need to consider two separate forms of the continuity equation. Following the analysis in [28] and [8], the continuity equation for a compressible fluid may be written in a divergence (or conservation) form

$$\frac{d\rho}{dt} = -\nabla \cdot (\rho \mathbf{u}) + \mathbf{u} \cdot \nabla \rho \quad (1)$$

or, by application of the product rule, a convective form

$$\frac{d\rho}{dt} = -\rho \nabla \cdot \mathbf{u}, \quad (2)$$

where $d/dt = \partial/\partial t + \mathbf{u} \cdot \nabla$ is the material derivative. By the product rule, (1) and (2) are equivalent in a continuous space; however, this is not necessarily true for their discrete forms [13]. Roughly speaking, the product rule is not necessarily satisfied for discrete divergence and gradient operators, which is discussed further in Section 3.1.

Recall that the first law of thermodynamics states that increments in heat Q and work W per unit mass lead to a change in the specific internal energy e_i as follows:

$$\frac{de_i}{dt} = \delta Q + \delta W. \quad (3)$$

Work per unit mass is defined as $\delta W = -pdv/dt$ where p is pressure and $v = \rho^{-1}$ is specific volume and the heat according to the second law of thermodynamics is $\delta Q = T \frac{ds}{dt}$ where T is temperature and s is specific entropy. With these definitions, we rewrite (3) as follows

$$T \frac{ds}{dt} = \frac{de_i}{dt} + p \frac{dv}{dt}. \quad (4)$$

Next, the equation of state (EOS) for an ideal gas $p = \rho RT$ may be written as

$$p = (\gamma - 1)\rho e_i \quad (5)$$

where we have invoked the Meyer relation for the mass-weighted specific gas constant $R = c_p - c_v$ and ratio of specific heats $\gamma = c_p/c_v$. Substituting (5) and $v = 1/\rho$ into (4) yields

$$\frac{de_i}{dt} - \frac{(\gamma - 1)e_i}{\rho} \frac{d\rho}{dt} = T \frac{ds}{dt}, \quad (6)$$

where the right-hand side represents entropy production. At this stage, we focus on a fluid with no molecular diffusion or thermal conduction (compressible Euler equations), so the entropy production is zero.

Since we need a prognostic equation for specific internal energy, the material time derivative of density needs to be eliminated in (6). Utilizing the convective form (2) yields the *Product Rule (PR) form*

$$\frac{\partial e_i}{\partial t} + \mathbf{u} \cdot \nabla e_i + (\gamma - 1) e_i \nabla \cdot \mathbf{u} = 0, \quad (7)$$

The second term in (7) represents the transport of specific internal energy, which reduces to temperature transport for a gas with uniform composition. The third term models the conversion of mechanical (kinetic) energy into internal energy, which is merely the standard pressure dilation $p \nabla \cdot \mathbf{u}$ normalized by density ρ . The SIEE (7) is particularly simple and only requires one additional term over the standard potential temperature equation used in traditional NWP DyCores.

By inserting (2) into (6) and setting $ds/dt = 0$ yields the *No Product Rule (No PR) form*

$$\frac{\partial e_i}{\partial t} + \mathbf{u} \cdot \nabla e_i + \frac{(\gamma - 1)e_i}{\rho} (\nabla \cdot (\mathbf{u}\rho) - \nabla \rho \cdot \mathbf{u}) = 0, \quad (8)$$

or *divergence form*. The normalized pressure dilation term in (8) involves the difference of a mass flux and density gradient terms. Although more complicated than the PR-form, (7)

is compatible with the conservative form of the continuity equation; as shown later, this PR form is able to conserve mass to machine precision.

2.3. Dynamical Forces: Pressure Gradient Force, Geopotential, and Coriolis Force

Adapting the momentum balance equation for HA applications poses several numerical challenges. The density ρ and pressure p decrease approximately exponentially with height z , such that both are ~ 10 orders of magnitude smaller at ~ 300 km than at the surface. Thus at high altitudes the pressure gradient term $\nabla p/\rho$ in the acceleration equation consists of the division of two very small quantities, which can be a source of numerical error [40].

Specifically, the pressure gradient force (PGF) per unit mass is given by

$$\mathbf{f}_{PGF} = -\frac{\nabla p}{\rho} \quad (9)$$

where pressure is given by the EOS (5). For a constant composition atmosphere, ρ and e_i vary, producing a quadratic nonlinearity in the pressure gradient factor. Since each of these prognostic variables is represented by a polynomial basis function, aliasing will occur once the gradient is discretized with the SEM (see Section 3.1) [28]. For regions of the atmosphere where γ varies, pressure possesses a cubic nonlinearity, which is an even greater source of aliasing error. Although the convective terms in the acceleration/momentum balance also possess quadratic/cubic nonlinearities, the division by density at high altitudes *magnifies* where the atmosphere is highly rarefied. Hence, we seek to mitigate this problem by expressing (9) using a logarithmic derivative with respect to density, which is also employed by other nonhydrostatic high-altitude models [40, 31].

Inserting the equation of state (5) into the PGF expression (9) and expanding via the product rule yields:

$$\begin{aligned} -\mathbf{f}_{PG} &= \frac{\nabla p}{\rho} = (\gamma - 1)e_i \frac{\nabla \rho}{\rho} + (\gamma - 1)\nabla e_i + e_i \nabla \gamma \\ &= (\gamma - 1)e_i \nabla \log \rho + (\gamma - 1)\nabla e_i + e_i \nabla \gamma. \end{aligned} \quad (10)$$

In the final expression on the right, there is no division by density via the incorporation of the density denominator into a log-density gradient term. An explicit call to the equation of state is eliminated since the pressure term disappears here. A logarithm and an additional gradient calculation are required; however, the pressure-gradient calculation is eliminated, so the additional cost is negligible. These simplifications come at the expense of having to compute a new specific-heat gradient $\nabla \gamma$ explicitly: previously when ∇p was calculated explicitly, this term was discretized implicitly by evaluating p using the equation of state. While this new $\nabla \gamma$ term vanishes in the lower atmosphere, it is non-zero in the variable composition thermosphere.

Height dependent gravity is also necessary for high-altitude applications where the acceleration of gravity is given by $g(z) = g_0(1 + z/a)^{-2}$ [24, Eq. (1.4)], where g_0 is the mean surface acceleration, a is the radius of the earth, and z is geometric altitude. Although

the acceleration of gravity also depends on latitude and longitude, these dependencies are neglected in this paper.

As discussed in 3.2, we observe superior numerical performance when the gravity term is expressed as the discrete gradient of the geopotential

$$\Phi(z) = \int_0^z g(z') dz' = \frac{g_0 z}{1 + z/a} = g_0 \mathfrak{z}, \quad (11)$$

where $\mathfrak{z} = \Phi(z)/g_0$ is the geopotential height. Under the shallow-atmosphere approximation, $\Phi(z) \approx g_0 z$. Finally, the Coriolis force is included without any traditional approximations via $-2\boldsymbol{\Omega} \times \mathbf{u}$ [24, Eq. (2.8)]. As a result, there is a component of the Coriolis force in the vertical acceleration equation.

2.4. Summary of Equation Sets

The continuity, acceleration, and SIEE in PR, or convective form, is expressed as

$$\frac{\partial \rho}{\partial t} + \nabla \rho \cdot \mathbf{u} + \rho \nabla \cdot \mathbf{u} = 0 \quad (12a)$$

$$\frac{\partial \mathbf{u}}{\partial t} + \mathbf{u} \cdot \nabla \mathbf{u} - \mathbf{f}_{PG} + \nabla \Phi + 2\boldsymbol{\Omega} \times \mathbf{u} = 0 \quad (12b)$$

$$\frac{\partial e_i}{\partial t} + \mathbf{u} \cdot \nabla e_i + (\gamma - 1) e_i \nabla \cdot \mathbf{u} = 0, \quad (12c)$$

where the mass normalized PGF is given by (10). Compared to the potential temperature equation set used in previous NUMA dynamical cores [27, 18], the energetic equation (12c) adds a single additional term, which is the normalized pressure dilation term. This term vanishes in the case of incompressible flow $\nabla \cdot \mathbf{u} = 0$.

The corresponding equation set in No-PR, or divergence form, is expressed as

$$\frac{\partial \rho}{\partial t} + \nabla \cdot (\rho \mathbf{u}) = 0 \quad (13a)$$

$$\frac{\partial \mathbf{u}}{\partial t} + \mathbf{u} \cdot \nabla \mathbf{u} - \mathbf{f}_{PG} + \nabla \Phi + 2\boldsymbol{\Omega} \times \mathbf{u} = 0 \quad (13b)$$

$$\frac{\partial e_i}{\partial t} + \mathbf{u} \cdot \nabla e_i + \frac{(\gamma - 1)e_i}{\rho} (\nabla \cdot (\mathbf{u}\rho) - \nabla \rho \cdot \mathbf{u}) = 0. \quad (13c)$$

In contrast to (12), there are two additional terms in (13c) to account for the normalized pressure dilation term. As shown numerically in Section 4, the divergence form of the continuity equation in (13) allows this equation set to conserve mass to machine precision.

3. Numerical Methods

3.1. Mimetic Spectral Element Method

The proposed SIEEs were implemented in two spectral element models: NUMA and NEPTUNE. NUMA is a research-oriented CFD code based on the element-based Galerkin (EBG) method on tensor-product elements, which are quadrilaterals in 2D and hexahedra in 3D [16]. NUMA supports both spectral element method (SEM) and discontinuous Galerkin (DG) methods in a unified framework [1] using both massive CPU clusters [38] and GPUs [2]. NEPTUNE is the U. S. Navy’s next-generation operational global atmospheric model appropriate for both limited-area and global weather prediction [39]. NEPTUNE utilizes the SEM for dynamics and the DG method for tracer transport. In this section, we give a very brief outline of the SEM spatial discretization used for the PR form (12) and No-PR (13) form of the SIEE. For additional details, the reader may consult [16] or [27].

Both NUMA and NEPTUNE use a mimetic SEM. The SEM decomposes the domain of interest Ω into a collection of N_e non-overlapping elements Ω^e . A *compatible* (or *mimetic*) SEM mimics fundamental vector calculus identities in a discrete sense [48]. For example, consider *Green’s identity* for sufficiently smooth f and \mathbf{u}

$$\int_{\Omega_e} \mathbf{u} \cdot \nabla f \, d\Omega_e + \int_{\Omega_e} f \nabla \cdot \mathbf{u} \, d\Omega_e = \int_{\Gamma_e} f \mathbf{u} \cdot \hat{\mathbf{n}} \, d\Gamma_e, \quad (14)$$

where $\hat{\mathbf{n}}$ is the outwardly facing unit normal vector and Γ_e is the boundary of Ω_e . A discrete analog of (14) is given by

$$\langle \mathbf{u} \cdot \nabla_d f \rangle_{\Omega_e} + \langle f \nabla_d \cdot \mathbf{u} \rangle_{\Omega_e} = \langle f \mathbf{u} \cdot \hat{\mathbf{n}} \rangle_{\Gamma_e},$$

where $\langle \cdot \rangle$ is discrete (inexact) integration. Inexact integration, which uses quadrature points that are coincident with interpolation nodes, is chosen in order to a) produce a diagonal mass matrix and b) reduce the computational complexity of the inviscid operators to $\mathcal{O}(N_e p^4)$, where p is the polynomial order. The discrete divergence and gradient operators on an element Ω^e are defined via

$$\nabla_d \cdot \mathbf{u} = \frac{1}{J} \sum_{\alpha=1}^3 \frac{\partial (J u^\alpha)}{\partial x^\alpha}$$

$$\nabla_d f = \sum_{\alpha=1}^3 \frac{\partial f}{\partial x^\alpha} \hat{\mathbf{e}}^\alpha$$

where u^α are the three contravariant components of velocity, $\hat{\mathbf{e}}^\alpha$ are the contravariant basis vectors that are oriented normally with respect to each element, and $J > 0$ is the determinant of the metric Jacobian matrix. For further details, the reader may consult Section 6.2 in [34].

Let $\psi_i(\mathbf{x})$ be a basis/test function constructed as a tensor product of Lagrange polyno-

mials. Following [1], define the finite dimensional function space

$$\mathcal{V}_N^{CG} = \{\psi \in H^1(\Omega) : \psi \in \mathcal{P}_N(\Omega_e)\}$$

where $H^1(\Omega) \subset C^0(\Omega)$ and \mathcal{P}_N is the space of N -th order polynomials. The continuity between elements Ω_e is enforced via the Direct Stiffness Summation (DSS) operator. We consider two categories of weak-forms illustrated via the PR form of the continuity equation (12a) and the No-PR continuity equation (13a). In the first case, termed the *strong variational weak form*, we merely multiply $\psi_i(\mathbf{x})$ by the governing equation and integrate over the domain Ω with boundary Γ . This is the weak form utilized in the NWP version of NEPTUNE [18]. In the second case, termed the *weak weak form*, an integration by parts (IBP) is performed, yielding

$$\int_{\Omega} \left[\psi_i \frac{\partial \rho}{\partial t} - \nabla \psi_i \cdot (\rho \mathbf{u}) \right] d\Omega + \int_{\Gamma} \psi_i \rho \mathbf{u} \cdot \hat{\mathbf{n}} d\Gamma = 0. \quad (16)$$

In all our tests, we enforce a no-mass flux (or rigid) BC on both the lower (ground) and upper boundaries where the normal velocity $w = \mathbf{u} \cdot \hat{\mathbf{n}}$ is set to zero. Hence, the surface integral in (16) vanishes as a result of imposing the rigid BC in a *weak sense*. In contrast, the rigid BCs must be enforced in a *strong sense* for the strong weak form by altering the prognostic vertical velocity w during dynamics.

3.2. Grid and Metric Terms

Both NUMA and NEPTUNE use an equi-angular cubed sphere [42, 41] spectral element grid for each horizontal level expressed in Cartesian coordinates. Let $\boldsymbol{\xi} = (\xi, \eta, \zeta) = (\xi_1, \xi_2, \xi_3)$ be the element local coordinates for each reference element (cube), and let $\mathbf{x} = (x, y, z) = (x_1, x_2, x_3)$ be the physical Cartesian coordinates in each physical element. Grids are constructed using concentric cubed-sphere spherical shells with spherical coordinates (r, ϕ, λ) , where r is the distance from the center of the earth, ϕ is latitude, and λ is longitude. By this construction $r = r(\zeta)$ and $\zeta = \zeta(r)$, while $(\phi, \lambda) = F(\xi, \eta)$ and $(\xi, \eta) = F^{-1}(\phi, \lambda)$. In NUMA, a Gal-Chen-Somerville terrain-following coordinate [14] is employed in the vertical by warping the computational grid. NEPTUNE utilizes a hybrid, height-based terrain-following coordinate that transitions from purely terrain following at the surface to a purely height-based at the model top [43].

Each hexahedral element is mapped onto a reference computational element (cube) via the mapping $\mathbf{x} = \mathbf{X}(\boldsymbol{\xi})$. In addition, a source term representing height-dependent gravitational acceleration must be constructed. These metrics must be constructed carefully in order to prevent spurious source terms from polluting the solution, which can result in model instability. The analysis in [33] and [35] provide a rigorous discussion of these metric terms and spurious noise terms from a DG viewpoint, while [34, Chapter 6] provides a spectral element (CG) analysis.

The standard method of computing the metric terms (the contravariant vectors) is using the cross-product of the covariant vectors resulting in Eq. (12.30) in [16] which are written

as

$$\nabla_{\xi^i} = \frac{1}{J} \left(\frac{\partial \mathbf{x}}{\partial \xi^j} \times \frac{\partial \mathbf{x}}{\partial \xi^k} \right) \quad (17)$$

where the determinant of the metric Jacobian is defined as $J = \frac{\partial \mathbf{x}}{\partial \xi} \cdot \left(\frac{\partial \mathbf{x}}{\partial \eta} \times \frac{\partial \mathbf{x}}{\partial \zeta} \right)$ and i, j, k are defined cyclically such that if $i = 1$, then $j = 2$, and $k = 3$, etc. Let us call the metric terms given in (17) the *cross-product* form. Since both NUMA and NEPTUNE use Cartesian coordinates, the cross-product form may not faithfully represent the spherical domain when coarse grids are used.

The *semi-analytic* metrics [54] addresses the deficiency by building the spherical geometry into the metric terms. We again use (17) but include the map from spherical to Cartesian coordinates as follows:

$$x = r \cos \phi \cos \lambda; \quad y = r \cos \phi \sin \lambda, \quad z = r \sin \phi \quad (18)$$

where $\phi \in [-\frac{\pi}{2}, +\frac{\pi}{2}]$ and $\lambda \in [0, 2\pi]$ denote the latitude and longitude and r is the radius. We can now use the chain rule as follows

$$\frac{\partial \mathbf{x}}{\partial \xi} = \frac{\partial \mathbf{x}}{\partial r} \frac{\partial r}{\partial \xi} + \frac{\partial \mathbf{x}}{\partial \phi} \frac{\partial \phi}{\partial \xi} + \frac{\partial \mathbf{x}}{\partial \lambda} \frac{\partial \lambda}{\partial \xi}$$

where terms such $\frac{\partial \mathbf{x}}{\partial r}$ are computed using (18). This approach is ideal on spherical domains; however, it may not be accurate if steep topography is present.

Finally, the *curl-invariant* (CI) metrics [33] are constructed to satisfy constant-state preservation, whereby a constant flow field remains unchanged as time evolves. These metrics are expressed as

$$\nabla_{\xi^i} = \frac{1}{2J} \left[\frac{\partial}{\partial \xi^k} \left(\frac{\partial \mathbf{x}}{\partial \xi^j} \times \mathbf{x} \right) - \frac{\partial}{\partial \xi^j} \left(\frac{\partial \mathbf{x}}{\partial \xi^k} \times \mathbf{x} \right) \right] \quad (19)$$

where, once again, the indices (i, j, k) are cyclic. Unlike the semi-analytic metrics, the CI metrics do not make any *a priori* assumptions on the grid or the presence of terrain. All three choices of metrics are available in NUMA, and we study how the choice of metrics impacts mass conservation and accuracy in Sec. 4.2. Our numerical experiments indicate that the gravitational acceleration must be represented as the numerical gradient of geopotential.

3.3. Time-Integration (TI) Methods

Both the PR SIEE (12) and no-PR SIEE (13), like all forms of the Euler equations, contain fast acoustic and gravity waves that must be treated carefully. NUMA uses both IMPLICIT-EXPLICIT (IMEX) [18] and Horizontally Explicit Vertically Implicit (HEVI) [15, 17] time-integration (TI) methods, while NEPTUNE relies solely on HEVI time-integration methods. In implicit-explicit (IMEX) methods, the right hand side of the governing equations is typically first linearized. The linear component is then solved implicitly in time, while the explicit component is solved explicitly. Physically, the fast waves are treated implicitly, while nonlinear slow waves are treated explicitly, thereby allowing a larger time step than a purely explicit method. Alternatively, we can avoid linearization of the implicit part but this

will require using a nonlinear solver (e.g., Newton’s method) [32]. The maximum time-step that maintains stability is constrained by the slow waves only. NUMA has flexible IMEX machinery [19], that may be used to construct efficient and flexible time integration (TI) schemes. IMEX schemes may either use a static reference state or a dynamically updated reference state. Both approaches are described below.

In the numerical experiments shown in Sec. 4, we use the second-order additive Runge-Kutta (ARK2b) time-integrator described in [18]. We have constructed two flavors of IMEX methods: 1) linearization over a fixed, hydrostatic reference state and 2) linearization over a previous time step. The latter is referred to as linear-HEVI (L-HEVI) [17] since this scheme is equivalent to a single Newton iteration of a fully implicit scheme or HEVI scheme [15, 55]. The L-HEVI scheme is similar to Rosenbrock schemes [51] and does not require an *a priori* reference field, making it appropriate for HA applications where the atmosphere undergoes very large changes in temperature and density. In addition, L-HEVI schemes have larger regions of stability than the standard IMEX scheme. Newton iterations are used to solve the nonlinear system of equations, and then a direct solve is used to do the linear solve. In particular, the Jacobian matrix is computed analytically, and LAPACK is used to solve the system. A Jacobian-Free Newton-Krylov (JFNK) algorithm was also tested, but a direct solve was found to be much faster. An extensive comparison is carried out in [17].

4. Low-Altitude Numerical Results

Our DyCore must be efficient and accurate for both tropospheric and HA simulations. Hence, our first two tests are low-altitude tests based on a baroclinic instability. We first implemented both the PR (12) and No-PR (13) equation sets in NUMA, which provides a flexible framework for testing the underlying numerics. The first test was the Ullrich baroclinic instability [53], which exercises the non-hydrostatic, deep-atmosphere, and variable-gravity aspects of the model. We then explored the model’s response to terrain using the Jablonowski-Williamson baroclinic instability test case [25].

4.1. Baroclinic Instability

A popular test case for deep-atmosphere, nonhydrostatic dynamical cores is the Ullrich baroclinic instability (BI) [53]. The background state for this case is an exact solution to the deep-atmosphere Euler equations that is in both hydrostatic and geostrophic balance [46]. Both height-dependent gravity and an exact form of the Coriolis force are assumed, which are also utilized in the NUMA dynamical core. A stream-function perturbation is superimposed on the basic state, which triggers a baroclinic instability and wave breaking after day 7. This case has been used for testing time-integrators such as nonlinear HEVI [15], the deep atmosphere version of MPAS [44], HA testing of the ICON general circulation model [5], and entropy-stable formulations of DG [56]. A moist version of this test case is included in the DCMIP 2016 suite [52].

We ran NUMA with 24 elements per cube sphere panel and $p = 4$ polynomials, which has an average horizontal resolution of 104 km at the equator and an equivalent angular resolution ~ 0.94 degrees along the equator (104 km at the surface). In the vertical, eight

vertical elements ($p = 4$) are used with the grid stretching specified in [53] with a model top of 30 km and a rigid boundary condition at both the lower and upper boundaries. A second-order, 1D IMEX time-integrator (ARK2) is used, where the linearization is performed over the previous time-step [17].

NUMA was run using both the no-PR and PR forms of the SIEE. A time-step of $\Delta t = 50.8235$ s is used with a no-Schur formulation with the PR form. This time-step may be increased to $\Delta t = 120$ s with the no-PR form. Fourth-order hyperdiffusion with a constant coefficient of $9 \times 10^{14} \text{m}^4/\text{s}$ is used to stabilize the dynamics in the horizontal. No hyperdiffusion or explicit filtering is utilized in the vertical; rather, NUMA relies on the implicit diffusion provided by the 1D IMEX TI to dissipate grid-point noise in the vertical.

Fig. 1 displays the surface pressure, 850 hPa temperature, and 850 hPa vorticity for day 8 (left) and day 10 (right) for the baroclinic instability as a function of latitude and longitude using the No-PR form. Corresponding results for the PR form are virtually indistinguishable except for day 10 of the surface pressure. In the PR form, the contours for surface pressure are noisier, indicating that there is less implicit diffusion near the surface in the No-PR form due to the weak imposition of the rigid BC. In addition, the surface pressure and 850 hPa contour plots in Figure 1 are in agreement with the corresponding results for MCore (Fig. 4 in [53]), ENDGame (Fig. 5 in [53]), and MPAS (Fig. 2 in [44]). There are observable differences between the displayed 850 hPa vorticity plots and those produced by MCore, ENDGame, and MPAS, indicating that this diagnostic is very sensitive to the choice of discretization, stabilization, and filtering.

As an additional verification, we ran an entropy-stable DG method in the ATUM code [56] using the same spatial resolution as NUMA. ATUM uses a conservative form of the total energy equation, which conserves both mass and total energy when used with a consistent DG method. Unlike NUMA and other spectral element models, ATUM does not require any additional stabilization in the form of hyper-diffusion. Like NUMA, ATUM also utilizes an ARK2b IMEX TI, which was run using a vertical Courant number of 3.0 and was run on a single NVIDIA V100-PCIE GPU. Since variable gravity is not implemented in ATUM, the initial condition of the BI was modified slightly to account for constant gravity. The surface pressure and 850 hPa temperature plots (not shown) were very similar to those shown in Fig. 1, while there were significant differences in the 850 hPa vorticity fields, especially at day 10. This is not surprising, since this field is sensitive to the stabilization and discretization scheme.

Figure 2 displays the minimum surface pressure (left panel) and the maximum horizontal wind speeds for the No-PR and PR forms of the SIEE and ATUM. As noted in [44], the minimum surface pressure diagnostic is relatively insensitive to discretization and the choice of parameters used in the stabilization scheme. Hence, there is good agreement between the two SIEE forms of NUMA, ATUM, and the seven nonhydrostatic and hydrostatic models shown in Fig. 3 in [44]. In contrast, the maximum horizontal velocities in panel b are sensitive to the choice of discretization. ATUM produces much larger horizontal velocities than either version of the SIEE. Comparing panel b of Fig. 2 to Fig. 4 in [44], the NUMA horizontal winds are similar in magnitude to the reference MPAS simulation, while the ATUM velocities

behave like the low-hyperdiffusion ($1 \times 10^{13} \text{ m}^4/\text{s}$) results presented in [44].

Figure 3 displays the relative mass loss time series for the No-PR and PR forms of the SIEE in NUMA. The total mass at any given time t is given by $M(t) = \int_{\Omega} \rho d\Omega$, and the relative mass loss is given by

$$\delta M(t) = \frac{|M(t) - M(0)|}{M(0)}. \quad (20)$$

For details on the numerical evaluation of the total mass, see Sec. 3.3 in [17]. The PR form does not conserve mass and hence produces a secular mass loss during the course of the simulation. In contrast, the No-PR form conserves mass to machine precision. This mass conservation results from using a conservative form of the continuity equation and a weak imposition of the rigid (no-flux) BC and because in SEM, the global integral of divergence is guaranteed to vanish even under inexact numerical integration.

Like most NWP and HA dynamical cores, the SIEE equation sets in NUMA are not designed to conserve total energy. As the BI evolves, internal and potential energies are transformed into kinetic energy (KE). NUMA and many other dynamical cores numerically dissipate this KE via artificial dissipation (e.g., hyper-diffusion). A useful diagnostic to study this energy transfer, proposed in [44], is a time series of the deviations of kinetic, internal, and potential energy, where these quantities are defined as

$$K = \frac{1}{2} \int_{\Omega} \rho (u^2 + v^2 + w^2) d\Omega \quad (21a)$$

$$I = \int_{\Omega} \rho e_i d\Omega \quad (21b)$$

$$P = \int_{\Omega} \rho \phi d\Omega \quad (21c)$$

where $\phi(z) = g_0 z / (1 + z/a)$ is the gravitational geopotential, g_0 is the acceleration of gravity at the earth's surface, and a is the radius of the earth. The mean specific values of these quantities are obtained by dividing by the total mass of the domain $M(t)$ with units J/kg, and the deviation is the difference from the initial value: $\Delta k = K(t)/M(t) - K(0)/M(0)$. ATUM, on the other hand, is designed to conserve total energy. Figure 4 displays these deviations in mean specific energy, along with the deviation in mean total energy for both the No-PR SIEE in NUMA and the corresponding time series for ATUM. The energy budget for the PR form in NUMA is nearly identical to the No-PR form, and are hence not displayed.

Until day 7, these energy deviations are very small for both models. After the onset of the instability at day 7, the flow becomes turbulent, producing positive kinetic energy and depleting the internal and potential energy. Similar to the MPAS result displayed in Fig. 5 of [44], there is a small decrease in total mean specific energy after day 8 since the dissipated kinetic energy is not accounted for in the total energy budget. Since ATUM does not dissipate kinetic energy, the total mean kinetic energy for ATUM is larger than NUMA. The small loss in mean specific total energy due to the dissipation of turbulent kinetic energy

by hyperviscosity for the NUMA simulation is comparable to the results report for MPAS [44] after 15 days of simulation. In contrast, the energy loss for ATUM is negligible.

4.2. Hydrostatic Baroclinic Instability with Terrain

Our second low-altitude test is the hydrostatic and geostrophic Jablonowski-Williamson baroclinic instability with a mean zonal flow of 20 m/s and no velocity perturbation [25]. Unlike the Ullrich BI, this test case includes an idealized globally-defined sinusoidal topography (see Eq. (7) in [25] for the geopotential definition). Although this test case is formulated for shallow-atmosphere, hydrostatic dynamical cores in a pressure-based vertical coordinate, it is straightforward to initialize this case in a terrain-following, height-based coordinate using Newton iteration. The purpose of this test is two-fold: 1) to verify that the No-PR form of the SIEE is stable and can conserve mass in the presence of topography and 2) to determine how the choice of metric terms influences mass conservation. These results are prerequisite for the high-altitude idealized mountain experiments in the next section.

This case was run at a low resolution of 6 elements per cube sphere panel and $p = 4$ polynomials with the ARK2 IMEX time-integrator with $\Delta t = 100$ s. Figure 5 shows a time series of the relative mass loss for the cross-product (Eq. (17)), semi-analytic, and curl-invariant (Eq. (19)) metrics after 30 days of integration. The upper BC is rigid for these tests and a terrain-following vertical coordinate is utilized with a mean vertical resolution of 1 km and mean equatorial horizontal resolution of 200 km with a model top at 30 km. Since the flow is hydrostatically and geostrophically balanced by the topography, no gravity waves are generated, so we found that a sponge BC is not necessary.

Figure 5 indicates that curl-invariant metrics conserve mass up to machine precision. There is no secular increase in mass-loss despite the presence of time-truncation error in the IMEX time-integrator. The simulation with the semi-analytic metrics produces a small mass-loss which increases with respect to time. Finally, the cross-product metrics produce an unacceptably large mass loss that is five orders of magnitude larger than the corresponding simulation with the semi-analytic metrics. This time series also has a secular increase in time. We note that the gradient of the geopotential in (13b) needs to be computed using the mimetic SEM; otherwise, mass conservation using the CI metrics is not ensured.

These results indicate that the No-PR form of the SIEE (13), when discretized with a mimetic SEM utilizing the curl-invariant metrics specified by (19), can conserve mass with or without topography. We have repeated this experiment with the ARS343 IMEX time-integrator [15] and seen similar results. Since curl-invariant metrics do not have any more computational overhead than the cross-product or semi-analytic metrics, these results indicate that the curl-invariant metrics are the preferred metrics for global-scale simulations on the sphere.

5. High-Altitude Numerical Results

We implemented the PR form of the SIEE set (12) in NEPTUNE and ran a series of HA tests. The first test is a steady-state balanced zonal flow with a user-specified temperature, specific gas, and ratio of specific heat profiles. This test case, which we designed for idealized

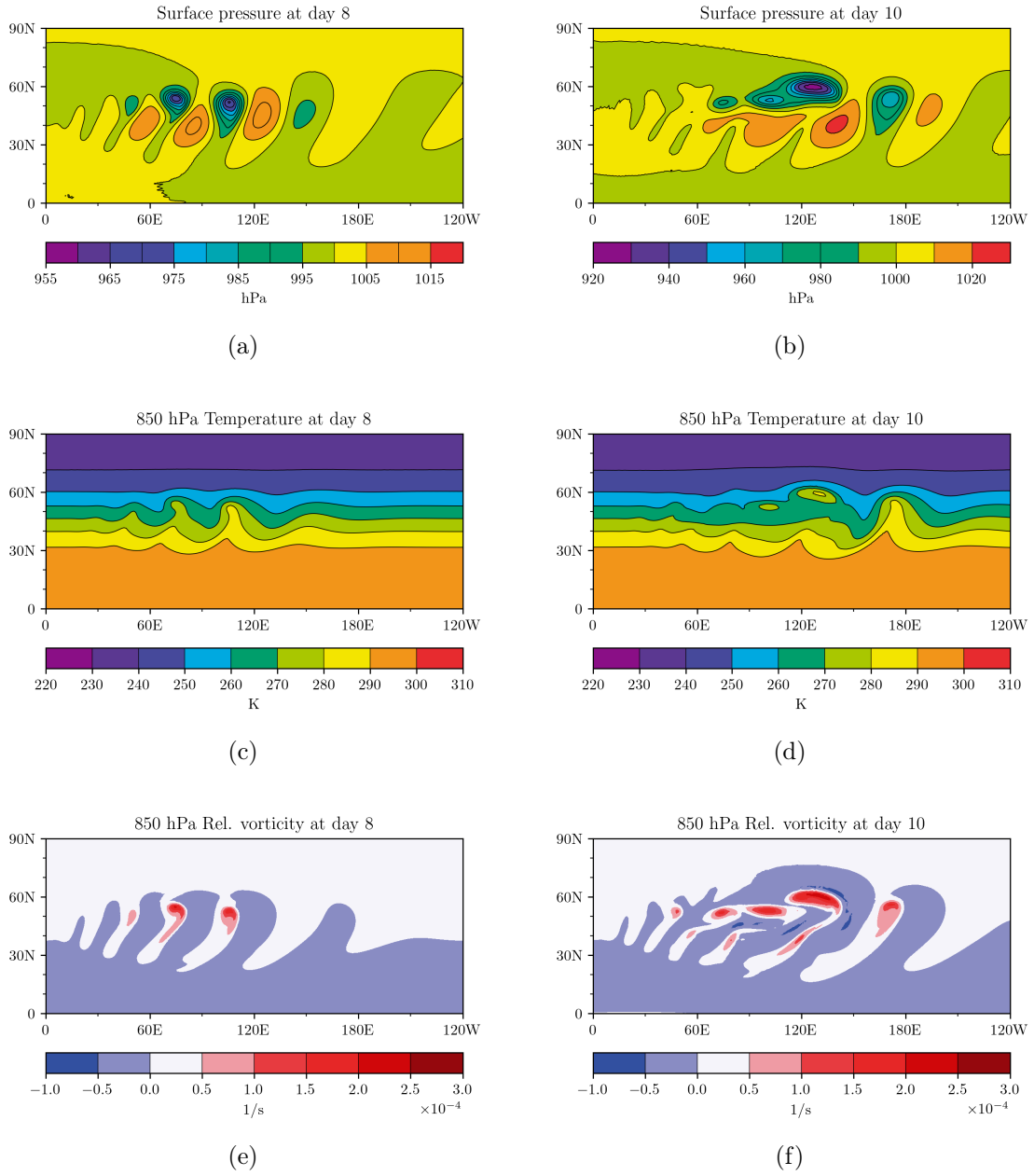


Figure 1: Surface pressure, 850 hPa temperature, and 850 hPa vorticity for day 8 (left) and day 10 (right) for NUMA using the No-PR formulation.

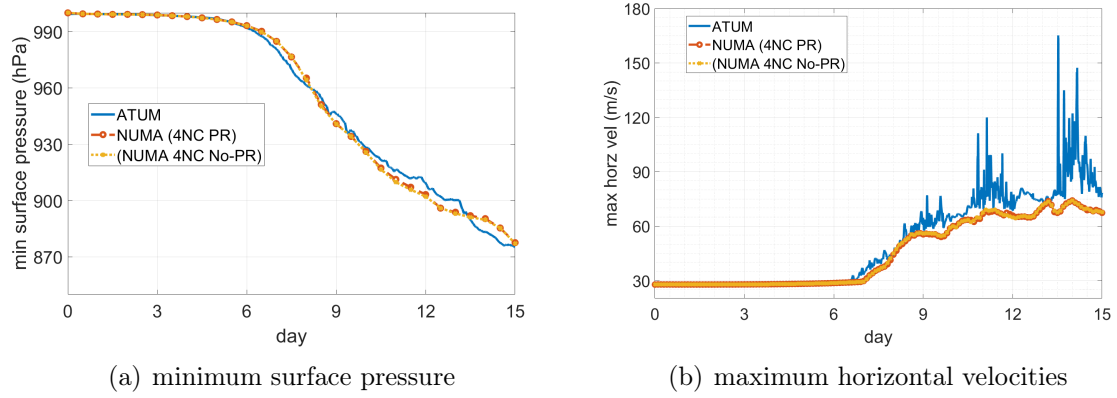


Figure 2: Minimum surface pressure (left) and maximum horizontal wind speeds (right) for the No-PR and PR forms in NUMA of the SIEE and ATUM.

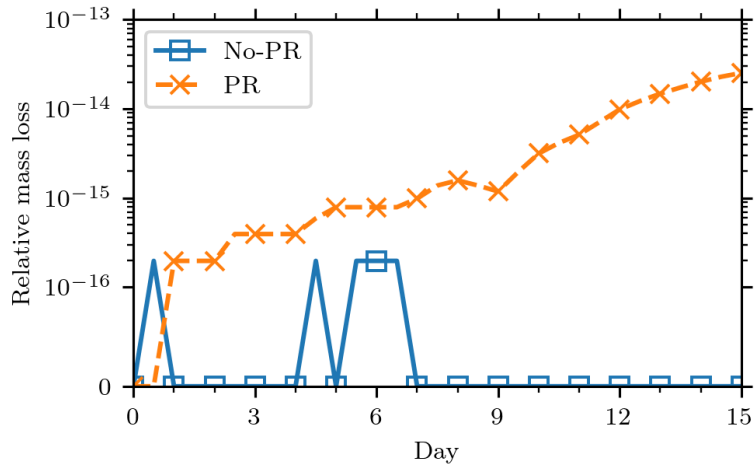


Figure 3: Relative mass loss time series for the No-PR and PR forms of the SIEE for the Ullrich BI test case in NUMA. The No-PR form of the SIEE conserves mass to machine precision.

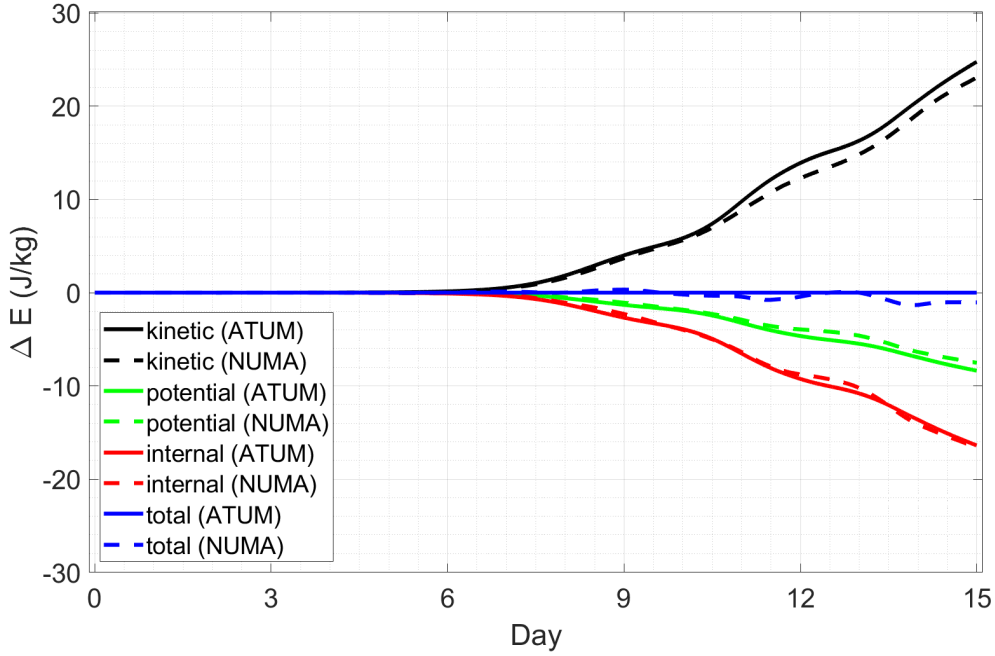


Figure 4: The deviation in mean specific energy for both the SIEE in NUMA and ATUM. The deviation for the No-PR and PR forms in NUMA are similar, so only the No-PR energy budget is displayed.

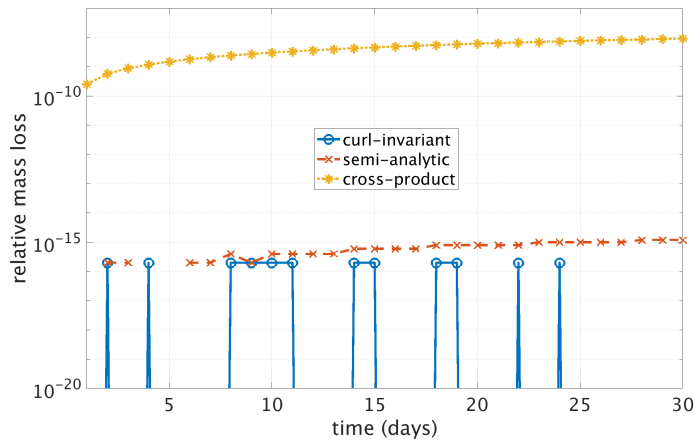


Figure 5: A time-series of the relative mass loss over 30 days of integration for the hydrostatic Jablonowski-Williams BI test case using the No-PR SIEE equation using three choices of metric tensors: cross-product, semi-analytic, and curl-invariant.

testing of a the Navy’s operational, hydrostatic NAVGEM model, allowed us to verify the equation set and stabilization settings in NEPTUNE. We then ran an orographic mountain wave test on the sphere [43] and validated these results using a linear Fourier ray method [11]. This orographic wave test demonstrated the equation set and NEPTUNE’s ability to resolve and transfer energy from the lower atmosphere into the thermosphere and the importance of variable composition in this process.

5.1. *Balanced Zonal Flow*

Our first HA test case is a steady-state solution to the deep-atmosphere, non-rotating, inviscid Euler equations where the temperature profile $T(z)$, specific gas profile $R(z)$, and the ratio of specific heats $\gamma(z)$ are allowed to vary in the vertical but not with respect to time [10]. The variation of the mass-weighted specific gas constant $R(z)$ is due to the variation in composition (molecular mass) with respect to height z [23]. Likewise, the variation of $\gamma(z)$ is due to the relative abundance of monoatomic, diatomic, and polyatomic species, where $\gamma(z)$ transitions from the diatomic limit of ~ 1.4 in the lower atmosphere to a monoatomic limit of ~ 1.66 in the upper atmosphere. Although a completely realistic model would include meridional variation in temperature and composition, as well as the effects of the Coriolis force, we are primarily interested in testing vertical aspects of NEPTUNE and NUMA to assess model stability for model tops in the thermosphere.

The analytic steady-state solution to this test case, derived in Sec. 5 of [10] using the compatibility relations presented in [57] for a non-rotating planet, consists of a zonal flow with a vertical shear

$$u(z, \phi) = u_{eq} \sqrt{\frac{R(z)T(z)}{R_0T_0}} \left(1 + \frac{z}{a}\right) \cos \phi \quad (22)$$

where $u_{eq} = 50$ m/s is a constant equatorial ground speed, $T_0 = T(0)$, $R_0 = R(0)$, and a is the radius of the earth. The corresponding balanced hydrostatic pressure is given by

$$p(z, \phi) = p_0 \exp \left(\frac{u_{eq}^2}{R_0T_0} F_2(z) \cos^2 \phi - \frac{u_{eq}^2}{2R_0T_0} \sin^2 \phi - F_1(z) \right) \quad (23)$$

where $F_2(z) = z/a + 1/2(z/a)^2$ and

$$F_1(z) = \int_0^z \frac{g(z')}{R(z')T(z')} dz' \quad (24)$$

and $g(z) = g_0(1 + z/a)^{-2}$ for height dependent gravity and $g(z) = g_0$ for constant gravity, where g_0 is the mean acceleration of gravity at sea level. The hydrostatic integral (24) reduces to $F_1(z) = z/H_\rho$ for an isothermal, constant composition, constant gravity atmosphere, where $H_\rho = RT_0/g_0$ is the scale height. The compatibility relations presented in [57] are derived from the steady-state meridional and zonal momentum balance equations for a deep, gravity-dependent atmosphere and do not make any assumption on the ratio of specific heats. In addition, the derivation of (22) and (23) is not dependent on γ , thus admitting a spatially-dependent $\gamma(z)$ profile.

Figure 6 displays the vertical profiles of a) temperature $T(z)$, specific gas constant $R(z)$, and ratio of specific heats $\gamma(z)$ generated by MSIS 2.0 [12] used in our numerical experiment with a model lid of 433 km. The temperature profile in panel a) broadly approximates the four layers of the atmosphere, reaching an exospheric temperature of 730 K in the upper thermosphere. Both $R(z)$ and $\gamma(z)$ are approximately constant below the mesopause at ~ 90 km, and then increase monotonically as the constituent species decrease in mass as height z increases. Since these profiles are specified numerically, the hydrostatic integral given by (24) must be evaluated via a numerical quadrature scheme consistent with the SEM. Appendix B describes such a consistent numerical method using recursive inexact integration that produces a discretely balanced hydrostatic pressure field.

NEPTUNE, using the PR form of the SIEE, was initialized with this steady state solution and run using 20 elements in the horizontal with $p = 4$ order polynomials, which yields an approximate horizontal resolution of $\overline{\Delta x} \approx 125$ km at the equator. A model top of 433 km with 46 elements and $p = 4$ in the vertical, yielding a 185 level stretched vertical grid. A nonlinear HEVI time-integrator utilizing the ARS343 scheme [15] with a time step $\Delta t = 60$ s is employed. Anisotropic hyperviscosity using the scheme proposed in [22] was applied to stabilize the SEM and a rigid lower and upper BC was applied. NEPTUNE was run for 10 days (240 hours), and the zonal, meridional, and vertical velocity perturbations are shown in Figure 6. Ideally, all velocity perturbations should be zero. This time series indicates that small discretization and aliasing errors accumulate during the first several hours of the simulation, yielding error in the horizontal and vertical velocities. The maximum velocity perturbations occurs near the upper boundary, where the small densities magnify and produce imbalances in both the vertical and horizontal. These numerical errors are then dissipated by the anisotropic diffusion scheme, producing a small, residual error at the end of the simulation.

Some numerical experimentation was required to reduce the discretization error in Figure 7. Although this test case is stable with a wide range of hyperdiffusion parameters, choosing too small of a parameter produces unacceptably large velocity perturbations. These perturbations are largest near the upper boundary since the density is very small in this region. Second, it was necessary to include the diffusive flux terms in the hyperdiffusion scheme at the lower and upper boundaries. These boundary terms, which result from performing integration by parts on the Laplacian operator, are proportional to the normal component of the gradient of each prognostic variable. Since the zonal velocity in (22) has a linear shear factor, this term must be accounted for to faithfully represent hyperdiffusion at the physical grid boundaries. We found that the numerical error illustrated in Figure 7 is sufficiently small to provide a stable background for subsequent tests. Once NEPTUNE was tuned for this steady-state test case, we then used these settings to run a mountain wave test case, presented in the next section.

5.2. Orographic Gravity-Wave Test Case

Our second HA test used the balanced zonal flow from the previous section as the background state for an orographic gravity-wave test. A balanced atmosphere with vertically varying temperature, specific gas constant, and ratio of specific heats was initialized using

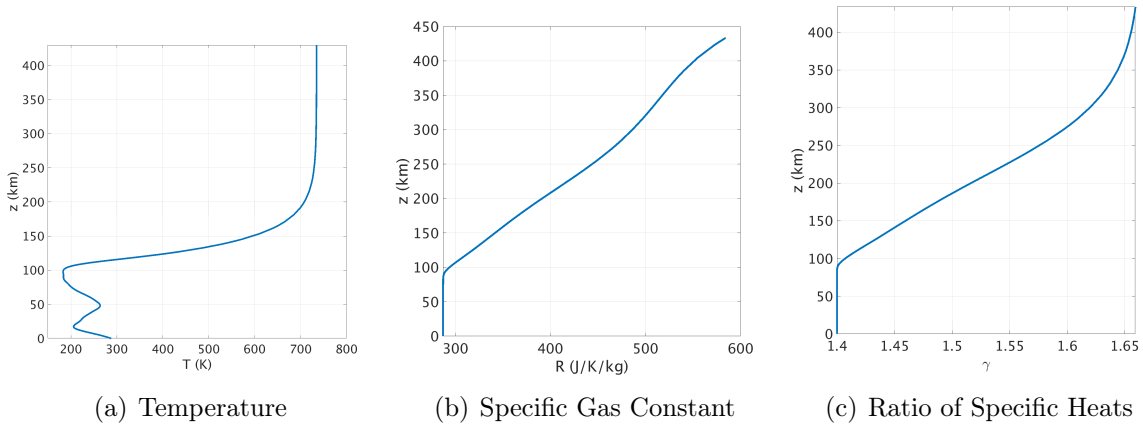


Figure 6: Vertical profiles of a) temperature $T(z)$, specific gas constant $R(z)$ and ratio of specific heats $\gamma(z)$ generated by MSIS 2.0 used in the steady-state balanced zonal flow test case and subsequent orographic wave test case.

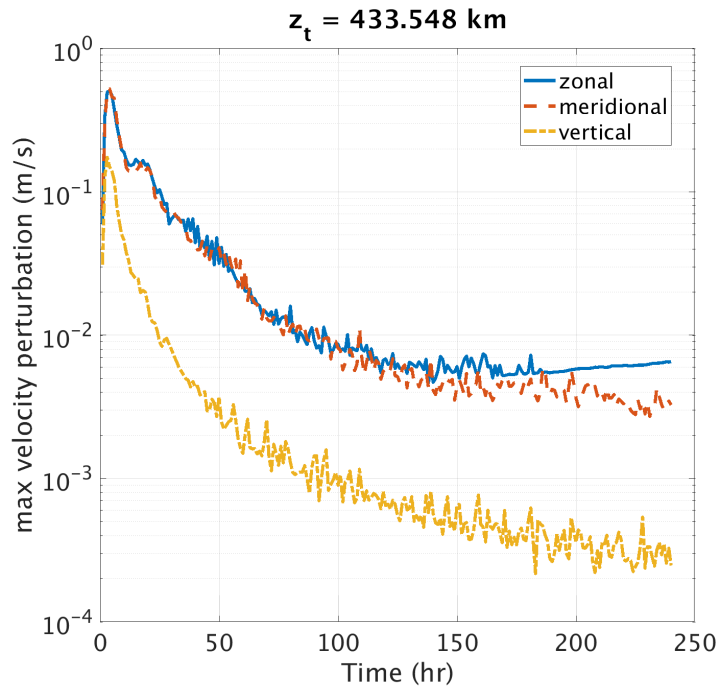


Figure 7: Time series of velocity perturbations for the balanced zonal flow test case specified by (22) and (23). Small discretization and aliasing errors accumulate during the first several hours of the simulation, yielding error in the horizontal and vertical velocities. These numerical errors are then dissipated by the anisotropic diffusion scheme.

the profiles displayed in Figure 6. The idealized terrain takes the analytical form

$$h(\lambda, \phi) = h_0 \exp \left[\frac{-r^2(\lambda, \phi)}{d_0^2} \right], \quad (25)$$

where $h_0 = 1$ m is the peak terrain height and $d_0 = 500$ km is the half-width of the Gaussian envelope. The great-circle distance from the mountain peak, centered at $(\lambda_c, \phi_c) = (\pi/4, 0)$, to any given point (λ, ϕ) is

$$r(\lambda, \phi) = a \arccos [\sin \phi_c \sin \phi + \cos \phi_c \cos \phi \cos (\lambda - \lambda_c)], \quad (26)$$

where a is the mean Earth radius. The large-scale Gaussian shape forces mountain-wave harmonics with horizontal wavelengths that can propagate freely in the vertical.

To prevent reflection of gravity waves off the upper boundary, an upper gravity wave implicit sponge [30] is utilized. The sponge depth is 156.27 km and the time-scale (inverse amplitude) is 0.125 s. In order to suppress initial transient waves, a transient sponge, similar to Eq. (26) in [31], is applied at all altitudes with time-dependent coefficients. Initially, this transient sponge is at full strength; as the simulation progresses, the sponge smoothly ramps down exponentially with respect to time as

$$\beta(z, t) = \beta_g(z) + \exp(-t/t_s)\beta_t(z) \quad (27)$$

where $\beta_g(z)$ is our standard gravity-wave-absorbing upper-level sponge,

$$\beta_t(z) = \beta_{tmax}^{-1} \sin^2 (\pi z / (2z_t)) \quad (28)$$

is an additional transient component that acts over the entire domain and targets acoustic waves, and $t_s = 5400$ s is the e-folding time scale that governs the ramp-down of the transient sponge. The time-scale (inverse amplitude) of β_{tmax} is 0.25 s.

This test was run with 24 elements per side of each cubed-sphere panel and the same vertical resolution and TI settings as the balanced zonal flow test. To ensure that all the gravity waves had sufficient time to propagate into the upper atmosphere, the test was run to 480 hours (20 days). Finally, a Richardson number based hyper-diffusion scheme was applied to suppress vertical grid-scale noise and control gravity wave breaking.

Figure 8 displays longitude-altitude cross sections along the equator of vertical velocity w for the orographic gravity-wave test case at a) 6 hours and b) 480 hours. The response at 6 hours is dominated by rapidly propagating acoustic waves, while panel b) shows a steady-state gravity wave response.

For comparison, we reran the gravity wave test with uniform composition. All other parameters were unchanged. Figure 9 displays corresponding cross-sections of vertical velocity at a) 6 hours and b) 480 hours. The magnitude of the gravity waves in Figure 9b are about two orders of magnitude larger and the horizontal wavelength is shorter compared to the variable composition case.

The difference in magnitude between the steady-state gravity wave patterns in these two

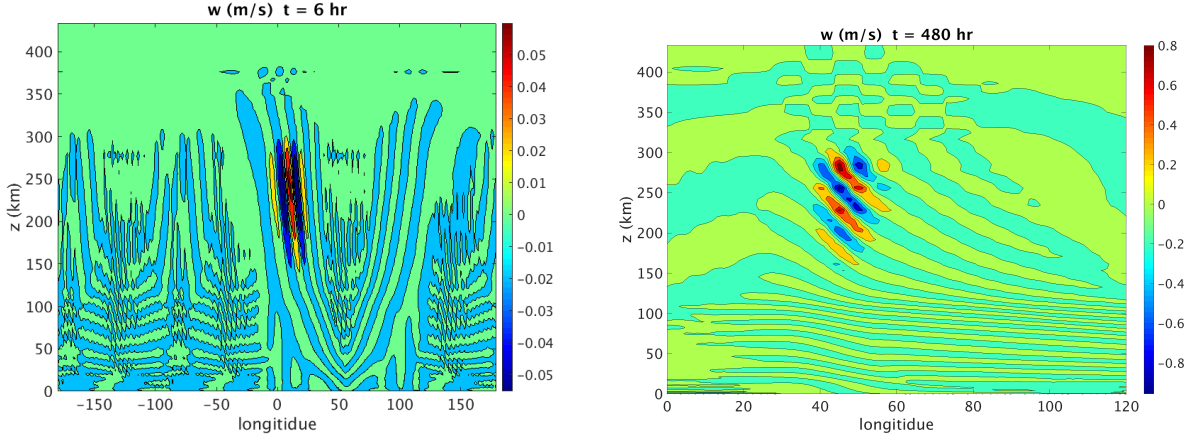


Figure 8: Longitude-Altitude cross sections along the equator of vertical velocity w for the orographic gravity-wave test case with variable composition at a) 6 hours and b) 480 hours. Panel a) is dominated by acoustic waves, while panel b) shows a steady-state gravity wave response.

simulations can be largely explained by the differences in the density scale height $H_\rho = (-\partial/\partial z \ln \rho)^{-1} \approx H/(1 + \partial H/\partial z)$, where $H = RT/g$ is the hydrostatic pressure scale height. In the uniform composition atmosphere, the scale height has a value close to 22 km above 150 km. In the variable composition scenario, the scale height increases from 22 km to over 45 km between 150 km and 300 km (the base of the implicit sponge). In the absence of molecular viscosity or thermal conductivity, the amplitude of vertically propagating gravity waves grow in proportion to $\exp(z/(2H))$, where z is the vertical propagation distance.

6. Energy Conservation

As shown in Section 4, the SIEE in No-PR form conserves mass but not total energy when inexact integration is utilized. In this section, we establish the condition under which total energy is conserved. First, define the kinetic, potential, and internal energy densities (or energy per unit volume):

$$\mathcal{K} = \frac{1}{2} \rho \mathbf{u} \cdot \mathbf{u} \quad (29a)$$

$$\mathcal{P} = \rho \Phi \quad (29b)$$

$$\mathcal{I} = \rho e_i. \quad (29c)$$

Integrating each of these densities over Ω yields the kinetic, potential, and internal energies defined by (21). If exact (spatial) integration and TI is used, then the product rule for the discrete gradient ∇_d holds and we are justified in taking the time-derivative of the three components of energy (21), yielding

$$\frac{\partial \mathcal{K}}{\partial t} = \left(\frac{1}{2} \mathbf{u} \cdot \mathbf{u} \right) \frac{\partial \rho}{\partial t} + \rho \mathbf{u} \cdot \frac{\partial \mathbf{u}}{\partial t} \quad (30a)$$

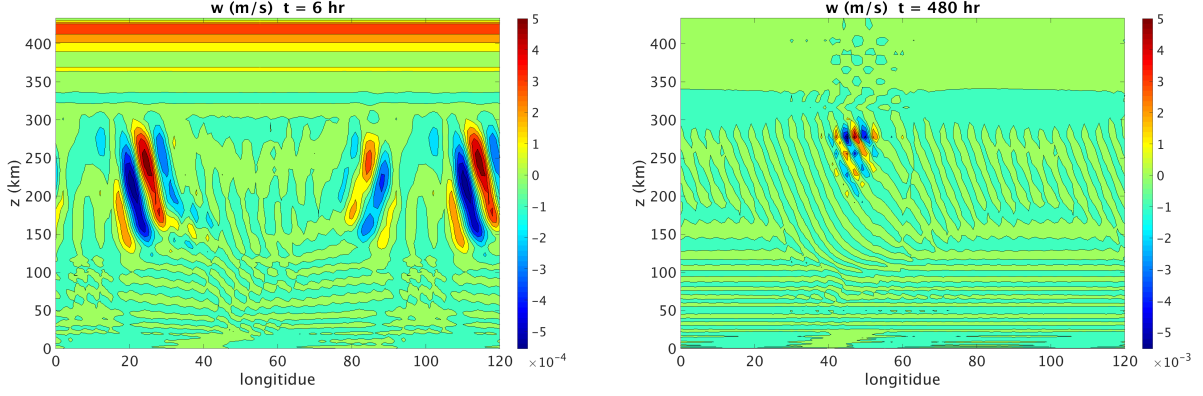


Figure 9: Longitude-Altitude cross sections along the equator of vertical velocity w for the orographic gravity-wave test case with uniform composition at a) 6 hours and b) 480 hours. Panel a) is dominated by acoustic waves, while panel b) shows a steady-state gravity wave response.

$$\frac{\partial \mathcal{P}}{\partial t} = \frac{\partial \rho}{\partial t} \Phi + \rho \frac{\partial \Phi}{\partial t} \quad (30b)$$

$$\frac{\partial \mathcal{I}}{\partial t} = \frac{\partial \rho}{\partial t} e_i + \rho \frac{\partial e_i}{\partial t}. \quad (30c)$$

Substituting the time-derivatives into (13) and summing yields

$$\begin{aligned} \frac{\partial (\mathcal{K} + \mathcal{P} + \mathcal{I})}{\partial t} = & - \left(\frac{1}{2} \mathbf{u} \cdot \mathbf{u} \right) [\nabla \cdot (\rho \mathbf{u})] - \rho \mathbf{u} \cdot [\mathbf{u} \cdot \nabla \mathbf{u}] - \mathbf{u} \cdot \nabla P - \rho \mathbf{u} \cdot \nabla \Phi \\ & - \Phi [\nabla \cdot (\rho \mathbf{u})] \\ & - e_i \nabla \cdot (\rho \mathbf{u}) - \rho \mathbf{u} \cdot \nabla e_i - (\gamma - 1) e_i [\nabla \cdot (\rho \mathbf{u}) - \nabla \rho \cdot \mathbf{u}] \end{aligned} \quad (31)$$

where we have listed the right-hand side rows to match which equation they come from (i.e., row 1 from (13a), row 2 from (13b), and row 3 from (13c)). Collecting terms in (31) gives

$$\begin{aligned} \frac{\partial (\mathcal{K} + \mathcal{P} + \mathcal{I})}{\partial t} = & - \nabla \cdot \left[\left(\frac{1}{2} \rho \mathbf{u} \cdot \mathbf{u} \right) \mathbf{u} \right] - \mathbf{u} \cdot \nabla p - \rho \mathbf{u} \cdot \nabla \Phi \\ & - \Phi \nabla \cdot (\rho \mathbf{u}) \\ & - \nabla \cdot [\rho e_i \mathbf{u}] - (\gamma - 1) \rho e_i \nabla \cdot \mathbf{u} \end{aligned} \quad (32)$$

where we have used the product rule in the last term; we can now see that this term is the pressure dilation term $P \nabla \cdot \mathbf{u}$. Collecting terms further yields

$$\begin{aligned} \frac{\partial (\mathcal{K} + \mathcal{P} + \mathcal{I})}{\partial t} = & - \nabla \cdot \left[\left(\frac{1}{2} \rho \mathbf{u} \cdot \mathbf{u} + \rho \Phi + \rho e_i \right) \mathbf{u} + p \mathbf{u} \right] \\ = & - \nabla \cdot [(\mathcal{K} + \mathcal{P} + \mathcal{I} + p) \mathbf{u}] \end{aligned} \quad (33)$$

which we can write in final form as

$$\frac{\partial E}{\partial t} = -\nabla \cdot [(E + p) \mathbf{u}]. \quad (34)$$

Equation (34) shows that the No-PR form of the SIEE satisfies conservation of total energy provided that exact integration is utilized. We note that the standard potential energy equation does not share this property.

7. Conclusion

- A HA DyCore based on a specific internal energy equation (SIEE) is proposed. A Product Rule (PR) and no Product Rule (no PR) form is discretized using the SEM and both an IMEX and HEVI time-integrator.
- The DyCore is verified for low-altitude using two baroclinic instability (BI) test cases that mimic tropospheric weather. HA tests using NEPTUNE are presented for both a steady-state balanced zonal flow and a mountain wave test case.
- When a no Product-Rule (No PR) continuity equation is used with a consistent IEE along with curl-invariant metrics and inexact integration, mass is conserved to machine precision with and without terrain. The PR form does not conserve mass using inexact integration.

Acknowledgments

Discussions with Jeremy Kozdon (NextSilicon), Sohail Reddy (Lawrence Livermore National Lab), and Simone Marras (Dept. of Mechanical and Industrial Engineering, New Jersey Institute of Technology) are acknowledged with pleasure. This work was funded by the Office of Naval Research Marine Meteorology and Space Weather program under grant # N0001419WX00721, and by the Defense Sciences Office of the Defense Applied Research and Projects Agency (DARPA DSO) through the Space Environment Exploitation (SEE) program.

Appendix A. Appendix: Recursive Inexact Integration

To numerically evaluate hydrostatic indefinite integrals like (24), we adopt the *recursive inexact integration* approach used in the ClimateMachine 2.0 (CLIMA) model [45] for maintaining hydrostatic balance. Evaluation of *definite integrals* within a CG framework using inexact integration is straightforward and efficient since quadrature points are collocated with interpolation points [16, Chapter 4] here. However, evaluation of indefinite integrals within an element-based Galerkin (EBG) framework is not straightforward. To illustrate why, let $f(x)$ be a continuous, real-valued function on the interval $[-1, 1]$, or the reference interval for a spectral element. Suppose we wish to evaluate the indefinite integral $F(x) = \int_{-1}^x f(z) dz$ at the set of LGL points x_i , where $1 \leq i \leq N$, where $N = p + 1$, p is the polynomial order,

and $x_1 = -1$ and $x_N = 1$. Letting $f_i = f(x_i)$, we approximate $f(x)$ in terms of Lagrange polynomials $h_i(x)$ with interpolation points x_i and integration weights ω_i . Note that

$$\begin{aligned}
F(x_N) &= \int_{-1}^1 f(z) dz \\
&= \sum_{i=1}^N f_i \int_{-1}^1 h_i(z) dz \\
&\approx \sum_{i=1}^N f_i \sum_{j=1}^N \omega_j h_i(x_j) \\
&\approx \sum_{i=1}^N f_i \omega_i
\end{aligned}$$

where we have used inexact integration in the third line and the cardinality property $h_i(x_j) = \delta_{i,j}$ in the fourth line, where $\delta_{i,j}$ is the Kronecker delta. If we replace the definite integral with an indefinite integral in this calculation, inexact integration cannot be used to evaluate $\int_{-1}^x h_i(z) dz$. Hence, we must construct a quadrature rule that is more accurate than inexact integration and hence appropriate for evaluation of (24).

Consider the sub-interval $E_i = [x_i, x_{i+1}]$ within the interval $[-1, 1]$, where $1 \leq i \leq (N-1)$. Let $R_i = (x_{i+1} - x_i)/2$ be the radius of E_i and let $m_i = (x_{i+1} + x_i)/2$ be the mid-point. We then construct a sequence of integration points that covers E_i via $x_{i,j} = R_i x_j + m_i$.

An indefinite integral is decomposed into a series of definite integrals via:

$$F(x_i) = \int_{-1}^{x_i} f(z) dz = \sum_{k=1}^{i-1} \int_{x_k}^{x_{k+1}} f(z) dz$$

These $(i-1)$ *definite* integrals are evaluated via inexact integration

$$\int_{x_k}^{x_{k+1}} f(z) dz = R_k \sum_{j=1}^N f_{k,j} \omega_j \tag{A.1}$$

where

$$f_{k,j} = f(x_{k,j}) = \sum_{m=1}^N f_m h_m(x_{k,j}) \tag{A.2}$$

and $f_m = f(x_m)$ are function values at the original set of LGL points x_m . Hence, we do *not* require additional data to evaluate the indefinite integral. However, note that there is no cardinality property for Lagrange polynomials in (A.2), implying that (A.1) requires evaluating a double sum.

References

- [1] D. S. ABDI AND F. X. GIRALDO, *Efficient construction of unified continuous and discontinuous Galerkin formulations for the 3d Euler equations*, J. Comput. Phys., 320 (2016), pp. 46–68.
- [2] D. S. ABDI, L. C. WILCOX, T. C. WARBURTON, AND F. X. GIRALDO, *A GPU-accelerated continuous and discontinuous Galerkin non-hydrostatic atmospheric model*, Int. J. High Perform. Comput. Appl., 33 (2019), pp. 81–109.
- [3] R. AKMAEV, *Whole atmosphere modeling: Connecting terrestrial and space weather*, Reviews of Geophysics, 49 (2011).
- [4] R. AKMAEV AND H.-M. JUANG, *Using enthalpy as a prognostic variable in atmospheric modelling with variable composition*, Quart. J. Roy. Meteor. Soc., 134 (2008), pp. 2193–2197.
- [5] S. BORCHERT, G. ZHOU, M. BALDAUF, H. SCHMIDT, G. ZÄNGL, AND D. REINERT, *The upper-atmosphere extension of the ICON general circulation model (version: uai-con-1.0)*, Geosci. Model Dev., 12 (2019), pp. 3541–3569.
- [6] S. BOUGHER, D. PAWLOWSKI, J. BELL, S. NELLI, T. MCDUNN, J. MURPHY, M. CHIZEK, AND A. RIDLEY, *Mars global ionosphere-thermosphere model: Solar cycle, seasonal, and diurnal variations of the mars upper atmosphere*, Journal of Geophysical Research: Planets, 120 (2015), pp. 311–342.
- [7] S. BOUGHER, A. RIDLEY, T. MAJEED, J. H. WAITE, R. GLADSTONE, AND J. BELL, *Development of the non-hydrostatic Jupiter global ionosphere thermosphere model (J-GITM): Status and current simulations*, 41st COSPAR Scientific Assembly, 41 (2016), pp. C3–2.
- [8] G. COPPOLA, F. CAPUANO, S. PIROZZOLI, AND L. DE LUCA, *Numerically stable formulations of convective terms for turbulent compressible flows*, J. Comput. Phys., 382 (2019), pp. 86–104.
- [9] Y. DENG, A. D. RICHMOND, A. J. RIDLEY, AND H.-L. LIU, *Assessment of the non-hydrostatic effect on the upper atmosphere using a general circulation model (GCM)*, Geophysical Research Letters, 35 (2008).
- [10] S. D. ECKERMANN, C. A. BARTON, AND J. F. KELLY, *Adaptation of θ -based dynamical cores for extension into the thermosphere using a hybrid virtual potential temperature*, Mon. Wea. Rev., 151 (2023), pp. 1937–1955.
- [11] S. D. ECKERMANN, D. BROUTMAN, J. MA, J. D. DOYLE, P.-D. PAUTET, M. J. TAYLOR, K. BOSSERT, B. P. WILLIAMS, D. C. FRITTS, AND R. B. SMITH, *Dynamics of orographic gravity waves observed in the mesosphere over the Auckland Islands*

- during the Deep Propagating Gravity Wave Experiment (DEEPWAVE), *J. Atmos. Sci.*, 73 (2016), pp. 3855–3876.
- [12] J. T. EMMERT, D. P. DROB, J. M. PICONE, D. E. SISKIND, M. JONES, JR., M. G. MLYNCZAK, P. F. BERNATH, X. CHU, E. DOORNBOS, B. FUNKE, L. P. GONCHARENKO, M. E. HERVIG, M. J. SCHWARTZ, P. E. SHEESE, F. VARGAS, B. P. WILLIAMS, AND T. YUAN, *NRLMSIS 2.0: A whole-atmosphere empirical model of temperature and neutral species densities*, *Earth and Space Science*, 8 (2021).
- [13] T. C. FISHER AND M. H. CARPENTER, *High-order entropy stable finite difference schemes for nonlinear conservation laws: Finite domains*, *J. Comput. Phys.*, 252 (2013), pp. 518–557.
- [14] T. GAL-CHEN AND R. C. SOMERVILLE, *On the use of a coordinate transformation for the solution of the Navier-Stokes equations*, *J. Comput. Phys.*, 17 (1975), pp. 209–228.
- [15] D. J. GARDNER, J. E. GUERRA, F. P. HAMON, D. R. REYNOLDS, P. A. ULLRICH, AND C. S. WOODWARD, *Implicit-explicit (IMEX) Runge-Kutta methods for non-hydrostatic atmospheric models*, *Geosci. Model Dev.*, 11 (2018), pp. 1497–1515.
- [16] F. X. GIRALDO, *An Introduction to Element-based Galerkin Methods on Tensor-Product Bases - Analysis, Algorithms, and Applications*, vol. 24 of *Texts in Computational Science and Engineering*, Springer, 2020.
- [17] F. X. GIRALDO, F. A. V. A. ALVES, J. F. KELLY, S. KANG, AND P. A. REINECKE, *A performance study of horizontally explicit vertically implicit (HEVI) time-integrators for non-hydrostatic atmospheric models*, *J. Comput. Phys.*, (under review) (2024), pp. 1–X.
- [18] F. X. GIRALDO, J. F. KELLY, AND E. M. CONSTANTINESCU, *Implicit-explicit formulations of a three-dimensional nonhydrostatic unified model of the atmosphere (NUMA)*, *SIAM Journal on Scientific Computing*, 35 (2013), pp. B1162–B1194.
- [19] F. X. GIRALDO, M. RESTELLI, AND M. LÄUTER, *Semi-implicit formulations of the Navier–Stokes equations: Application to nonhydrostatic atmospheric modeling*, *SIAM Journal on Scientific Computing*, 32 (2010), pp. 3394–3425.
- [20] D. GRIFFIN AND J. THUBURN, *Numerical effects on vertical wave propagation in deep-atmosphere models*, *Quarterly Journal of the Royal Meteorological Society*, 144 (2018), pp. 567–580.
- [21] D. J. GRIFFIN, *The Extension of a Non-Hydrostatic Dynamical Core into the Thermosphere*, PhD thesis, University of Exeter, 2018.
- [22] O. GUBA, M. A. TAYLOR, P. A. ULLRICH, J. R. OVERFELT, AND M. N. LEVY, *The spectral element method (SEM) on variable-resolution grids: Evaluating grid sensitivity and resolution-aware numerical viscosity*, *Geosci. Model Dev.*, 7 (2014), pp. 2803–2816.

- [23] J. K. HARGREAVES, *The Solar–Terrestrial Environment: An Introduction to Geospace: The Science of the Terrestrial Upper Atmosphere, Ionosphere, and Magnetosphere*, Cambridge University Press, 1992.
- [24] J. R. HOLTON, *An Introduction to Dynamic Meteorology*, Academic Press, San Diego, 4 ed., 1992.
- [25] C. JABLONOWSKI AND D. L. WILLIAMSON, *A baroclinic instability test case for atmospheric model dynamical cores*, Quarterly Journal of the Royal Meteorological Society, 132 (2006), pp. 2943–2975.
- [26] D. R. JACKSON, T. J. FULLER-ROWELL, D. J. GRIFFIN, M. J. GRIFFITH, C. W. KELLY, D. R. MARSH, AND M.-T. WALACH, *Future directions for whole atmosphere modeling: Developments in the context of space weather*, Space Weather, 17 (2019), pp. 1342–1350.
- [27] J. F. KELLY AND F. X. GIRALDO, *Continuous and discontinuous galerkin methods for a scalable three-dimensional nonhydrostatic atmospheric model: Limited-area mode*, J. Comput. Phys., 231 (2012), pp. 7988–8008.
- [28] C. A. KENNEDY AND A. GRUBER, *Reduced aliasing formulations of the convective terms within the Navier–Stokes equations for a compressible fluid*, J. Comput. Phys., 227 (2008), pp. 1676–1700.
- [29] J. KLEMP AND W. SKAMAROCK, *A constant pressure upper boundary formulation for models employing height-based vertical coordinates*, Mon. Wea. Rev., 150 (2022), pp. 2175–2186.
- [30] J. B. KLEMP, J. DUDHIA, AND A. D. HASSIOTIS, *An upper gravity-wave absorbing layer for NWP applications*, Mon. Wea. Rev., 136 (2008), pp. 3987–4004.
- [31] J. B. KLEMP AND W. C. SKAMAROCK, *Adapting the MPAS dynamical core for applications extending into the thermosphere*, Journal of Advances in Modeling Earth Systems, 13 (2021), p. e2021MS002499.
- [32] D. A. KNOLL AND D. E. KEYES, *Jacobian-free Newton–Krylov methods: A survey of approaches and applications*, J. Comput. Phys., 193 (2004), pp. 357–397.
- [33] D. A. KOPRIVA, *Metric identities and the discontinuous spectral element method on curvilinear meshes*, Journal of Scientific Computing, 26 (2006), pp. 301–327.
- [34] ———, *Implementing Spectral Methods for Partial Differential Equations: Algorithms for Scientists and Engineers*, Springer Science & Business Media, 2009.
- [35] D. A. KOPRIVA, F. J. HINDENLANG, T. BOLEMANN, AND G. J. GASSNER, *Free-stream preservation for curved geometrically non-conforming discontinuous Galerkin spectral elements*, Journal of Scientific Computing, 79 (2019), pp. 1389–1408.

- [36] P. KORN AND L. LINARDAKIS, *A conservative discretization of the shallow-water equations on triangular grids*, J. Comput. Phys., 375 (2018), pp. 871–900.
- [37] S. MARRAS, J. F. KELLY, M. MORAGUES, A. MÜLLER, M. A. KOPERA, M. VÁZQUEZ, F. X. GIRALDO, G. HOUZEAUX, AND O. JORBA, *A review of element-based Galerkin methods for numerical weather prediction: Finite elements, spectral elements, and discontinuous Galerkin*, Archives of Computational Methods in Engineering, 23 (2016), pp. 673–722.
- [38] A. MUELLER, M. A. KOPERA, S. MARRAS, L. C. WILCOX, T. ISAAC, AND F. X. GIRALDO, *Strong scaling for numerical weather prediction at petascale with the atmospheric model NUMA*, Int. J. High Perform. Comput. Appl., 33 (2019), pp. 411–426.
- [39] A. REINECKE, K. VINER, J. DOYLE, S. GABERSEK, M. MARTINI, J. MICHALAKES, D. RYGLICKI, D. FLAGG, AND F. GIRALDO, *Development and testing of a next generation spectral element model for the US Navy*, 17th Workshop on High Performance Computing (ECMWF), 24–28 October, Reading, UK, (2016).
- [40] A. RIDLEY, Y. DENG, AND G. TOTH, *The Global Ionosphere–Thermosphere Model*, Journal of Atmospheric and Solar-Terrestrial Physics, 68 (2006), pp. 839–864.
- [41] C. RONCHI, R. IACONO, AND P. S. PAOLUCCI, *The “cubed sphere”: A new method for the solution of partial differential equations in spherical geometry*, J. Comput. Phys., 124 (1996), pp. 93–114.
- [42] R. SADOURNY, *Conservative finite-difference approximations of the primitive equations on quasi-uniform spherical grids*, Mon. Wea. Rev., 100 (1972), pp. 136–144.
- [43] C. SCHÄR, D. LEUENBERGER, O. FUHRER, D. LÜTHI, AND C. GIRARD, *A new terrain-following vertical coordinate formulation for atmospheric prediction models*, Mon. Wea. Rev., 130 (2002), pp. 2459–2480.
- [44] W. C. SKAMAROCK, H. ONG, AND J. B. KLEMP, *A fully compressible nonhydrostatic deep-atmosphere equations solver for MPAS*, Mon. Wea. Rev., 149 (2021), pp. 571–583.
- [45] A. SRIDHAR, Y. TISSAOUI, S. MARRAS, Z. SHEN, C. KAWCZYNSKI, S. BYRNE, K. PAMNANY, M. WARUSZEWSKI, T. H. GIBSON, J. E. KOZDON, ET AL., *Large-eddy simulations with climatemachine v0. 2.0: A new open-source code for atmospheric simulations on GPUs and CPUs*, Geosci. Model Dev., (2021), pp. 1–41.
- [46] A. STANIFORTH AND A. WHITE, *Further non-separable exact solutions of the deep-and shallow-atmosphere equations*, Atmospheric Science Letters, 12 (2011), pp. 356–361.
- [47] A. STANIFORTH AND A. WHITE, *Forms of the thermodynamic energy equation for moist air*, Quart. J. Roy. Meteor. Soc., 145 (2019), pp. 386–393.

- [48] M. A. TAYLOR AND A. FOURNIER, *A compatible and conservative spectral element method on unstructured grids*, J. Comput. Phys., 229 (2010), pp. 5879–5895.
- [49] J. THUBURN, *Some conservation issues for the dynamical cores of NWP and climate models*, J. Comput. Phys., 227 (2008), pp. 3715–3730.
- [50] H. TOMITA AND M. SATOH, *A new dynamical framework of nonhydrostatic global model using the icosahedral grid*, Fluid Dynamics Research, 34 (2004), p. 357.
- [51] P. ULLRICH AND C. JABLONOWSKI, *Operator-split Runge–Kutta–Rosenbrock methods for nonhydrostatic atmospheric models*, Mon. Wea. Rev., 140 (2012), pp. 1257–1284.
- [52] P. A. ULLRICH, C. JABLONOWSKI, J. KENT, P. H. LAURITZEN, R. NAIR, K. A. REED, C. M. ZARZYCKI, D. M. HALL, D. DAZLICH, R. HEIKES, ET AL., *DCMIP2016: a review of non-hydrostatic dynamical core design and intercomparison of participating models*, Geosci. Model Dev., 10 (2017), pp. 4477–4509.
- [53] P. A. ULLRICH, T. MELVIN, C. JABLONOWSKI, AND A. STANIFORTH, *A proposed baroclinic wave test case for deep-and shallow-atmosphere dynamical cores*, Quarterly Journal of the Royal Meteorological Society, 140 (2014), pp. 1590–1602.
- [54] K. VINER, P. A. REINECKE, S. GABERSEK, D. D. FLAGG, J. D. DOYLE, M. MARTINI, D. RYGLICKI, J. MICHALAKES, AND F. GIRALDO, *Development of a three-dimensional spectral element model for NWP: Idealized simulations on the sphere*, in AGU Fall Meeting Abstracts, vol. 2016, 2016, pp. A31A–0004.
- [55] C. J. VOGL, A. STEYER, D. R. REYNOLDS, P. A. ULLRICH, AND C. S. WOODWARD, *Evaluation of implicit-explicit additive Runge-Kutta integrators for the HOMME-NH dynamical core*, J. Adv. Model. Earth Syst., 11 (2019), pp. 4228–4244.
- [56] M. WARUSZEWSKI, J. E. KOZDON, L. C. WILCOX, T. H. GIBSON, AND F. X. GIRALDO, *Entropy stable discontinuous Galerkin methods for balance laws in non-conservative form: Applications to Euler with gravity*, J. Comput. Phys., 468 (2022), p. 111507.
- [57] A. WHITE AND A. STANIFORTH, *A generalized thermal wind equation and some non-separable exact solutions of the flow equations for three-dimensional spherical atmospheres*, Quarterly Journal of the Royal Meteorological Society, 134 (2008), pp. 1931–1939.
- [58] N. WOOD, A. STANIFORTH, A. WHITE, T. ALLEN, M. DIAMANTAKIS, M. GROSS, T. MELVIN, C. SMITH, S. VOSPER, M. ZERROUKAT, ET AL., *An inherently mass-conserving semi-implicit semi-Lagrangian discretization of the deep-atmosphere global non-hydrostatic equations*, Quarterly Journal of the Royal Meteorological Society, 140 (2014), pp. 1505–1520.

- [59] E. D. ZARON, B. S. CHUA, P. A. REINECKE, J. MICHALAKES, J. D. DOYLE, AND L. XU, *The tangent-linear and adjoint models of the NEPTUNE dynamical core*, *Tellus: Series A*, 74 (2022).